

Chandra Phase-Resolved X-ray Spectroscopy of the Crab Pulsar

Martin C. Weisskopf ¹, Stephen L. O'Dell ¹, Frits Paerels ², Ronald F. Elsner ¹, Werner Becker ³, Allyn F. Tennant ¹, and Douglas A. Swartz ⁴

ABSTRACT

We present the first phase-resolved study of the X-ray spectral properties of the Crab Pulsar that covers all pulse phases. The superb angular resolution of the *Chandra* X-ray Observatory enables distinguishing the pulsar from the surrounding nebulosity, even at pulse minimum. Analysis of the pulse-averaged spectrum measures interstellar X-ray extinction due primarily to photoelectric absorption and secondarily to scattering by dust grains in the direction of the Crab Nebula. We confirm previous findings that the line-of-sight to the Crab is underabundant in oxygen, although more-so than recently measured. Using the abundances and cross sections from Wilms, Allen & McCray (2000) we find $[O/H] = (3.33 \pm 0.25) \times 10^{-4}$. Analysis of the spectrum as a function of pulse phase measures the low-energy X-ray spectral index even at pulse minimum — albeit with large statistical uncertainty and we find marginal evidence for variations of the spectral index. The data are also used to set a new ($3 - \sigma$) upper limit to the temperature of the neutron star of $\log T_{\infty} < 6.30$.

Subject headings: atomic processes — ISM: general — stars: individual: Crab Nebula — techniques: spectroscopic — X-rays: stars

1. Introduction

The Crab Nebula and Pulsar constitute an intricate system, observed throughout the electromagnetic spectrum. Due to the complex X-ray structure of the inner nebula and pulsar, the unprecedented angular resolution of the *Chandra X-ray Observatory* has proven

¹Space Science Department, NASA Marshall Space Flight Center, SD50, Huntsville, AL 35812

²Columbia Astrophysics Laboratory and Physics Department, Columbia University, New York, NY 10027

³Max Planck Institut für Extraterrestrische Physik, 85740 Garching bei München, Germany

⁴Universities Space Research Association, NASA Marshall Space Flight Center, SD50, Huntsville, AL 35812

invaluable in probing the nature of this region. In Weisskopf et al. (2000), we presented a HETGS (High-Energy Transmission Grating Spectrometer) zeroth-order image showing the complex morphology of the inner nebula, revealing the previously undiscovered X-ray inner ring between the pulsar and the X-ray torus. In Tennant et al. (2001), our phase-resolved analysis of an LETGS (Low-Energy Transmission Grating Spectrometer) zeroth-order image discovered significant X-ray emission from the pulsar in its “off” phase. Here we report our analysis of an LETGS dispersed image, to obtain phase-resolved X-ray spectroscopy of the Crab Pulsar.

After briefly describing the observation and data reduction (§2), we discuss the analysis of the measured spectrum (§3). In particular, we address photoelectric absorption and interstellar abundances (§3.1), impacts on the spectroscopy after allowing for scattering and various abundances and cross-sections (§3.2), comparison of our results with certain other measurements (§3.3), variation of the nonthermal spectrum with pulse phase (§3.4), and constraints on the temperature of the underlying neutron star (§3.5). Finally, we briefly summarize the results (§4).

2. Observation and Data Reduction

On 2000 February 2, we obtained a nominally 50-ks observation (ObsID 759) of the Crab Pulsar, with *Chandra*’s Low-Energy Transmission Grating (LETG) and High-Resolution Camera spectroscopy detector (HRC-S) — the LETGS. We examined the data after *Chandra* X-ray Center (CXC) pipeline processing and sorted events into an image binned in HRC pixels. Using LEXTRACT (developed by one of us, AFT) we extracted the pulsar’s dispersed spectrum from the image. The extraction uses a 29-pixel-wide (cross-dispersive) band centered on the pulsar, in 2-pixel (dispersive) increments. For the LETG’s 0.9912- μm grating period and 8.638-m Rowland-circle radius, the LETGS dispersion is 1.148 $\text{\AA}/\text{mm}$. Consequently, the spectral resolution of the binned data (two 6.4294- μm HRC-S pixels) is 0.01476 \AA . We combined positive and negative orders.

For estimating background, we similarly extracted reduced data from two 100-pixel-wide bands, starting 30 pixels to either side of the pulsar’s dispersed image (Fig. 1). We restricted all spectral analysis to the (first-order) energy range 0.3-to-4.2 keV. The upper spectral limit avoids contamination from the zeroth-order nebular image; the lower limit minimizes contamination from higher orders.

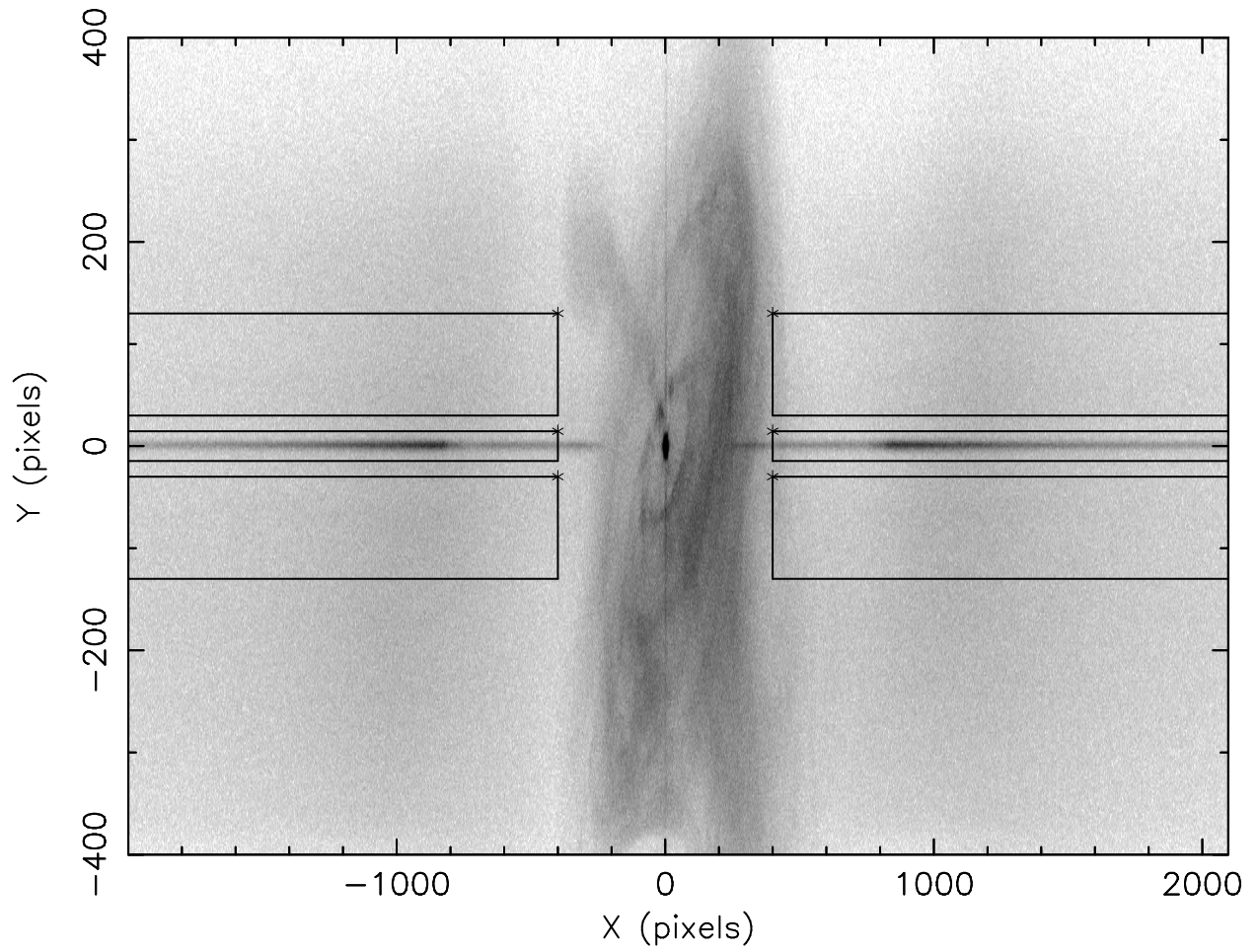


Fig. 1.— LETGS image of the Crab showing the dispersed spectrum. The rectangular boxes (discussed in the text) delineate regions selected for analysis. The image is stretched vertically for clarity.

3. Analysis and Results

We analyzed the data using the XSPEC (v.11.2) spectral-fitting package (Arnaud 1996). To ensure applicability of the χ^2 statistic, we merged spectral bins as needed to obtain at least 100 counts per fitting bin (before background subtraction). The merging results in no change in spectral resolution for the data above 0.67 keV and the merging of no more than three bins for the data above 0.5 keV. We utilized an effective area (Fig. 2) that includes the LETG energy-dependent efficiency to 10 spectral orders (Jeremy Drake, private communication; see also <http://asc.harvard.edu/cal/Letg/>).

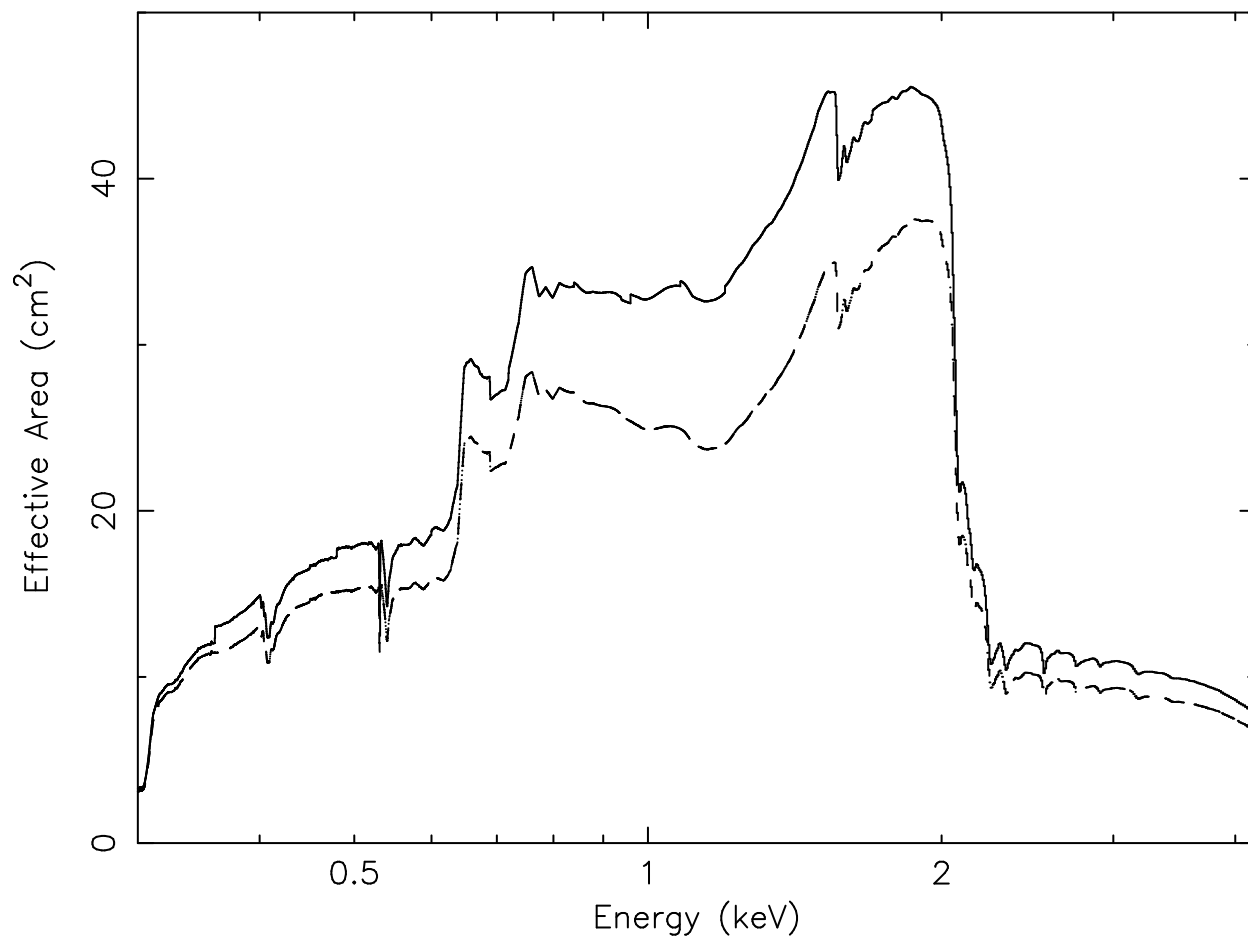


Fig. 2.— LETGS effective area versus energy over the band of interest. The solid line sums 10 (+ and -) spectral orders; the dashed line is the first-order contribution.

3.1. Broadband Spectrum — Initial Analysis

We first used XSPEC to fit the spectral data, independent of pulse phase, in the 0.3–4.2-keV band, using a power-law model with abundances `angr` (from Anders & Grevesse 1989) and absorption cross-sections `bcmc` (from Baluncinska-Church & McCammon 1992, with He cross-section from Yan, Sagdehpour, & Dalgarno 1998). Previous analyses of X-ray spectra — including the recent analysis of XMM-Newton EPIC-MOS observations of the Crab (Willingale et al. 2001) — use this combination (XSPEC `angr` & `bcmc`), which we denote as “Model 1”. The fit of the *Chandra* LETGS data to Model 1 (Fig. 3; Table 1 entry 1) is statistically unacceptable, yielding $\chi^2 = 1722$ on 1553 degrees of freedom.

Recognizing that the Model-1 residuals are largest near the O_K edge (0.532 keV), we thawed the relative abundance of oxygen, holding fixed that of the remaining elements. This “Model 2” (XSPEC `angr` & `bcmc`, with thawed O abundance) leads to a statistically acceptable fit (Fig. 4; Table 1 entry 2) — $\chi^2 = 1546$ on 1552 degrees of freedom. Table 1 lists the best-fit parameters and associated ($1\text{-}\sigma$) statistical errors, determined from extrema on single-parameter confidence contours. Because statistical parameter estimation is valid only if the null hypothesis is true, we omit “best-fit” parameters and errors for poor fits.

The Model-2 best-fit power-law photon index for the pulsar — $\Gamma_{\text{P}} = 1.596 \pm 0.020$ — is less (i.e., harder) than for the nebula and similar to previous measurements ($\Gamma_{\text{P}} = 1.5 \pm 0.1$, Toor & Seward 1974, 1977; $\Gamma_{\text{P}} = 1.60 \pm 0.02$, Massaro et al. 2000) of the Crab Pulsar spectrum. Before comparing in more detail (§3.3) our results with those of other observations, we first examine (§ 3.2) the influence on spectral fits of using different cross-section and absorption models within XSPEC and of including effects due to scattering by interstellar grains.

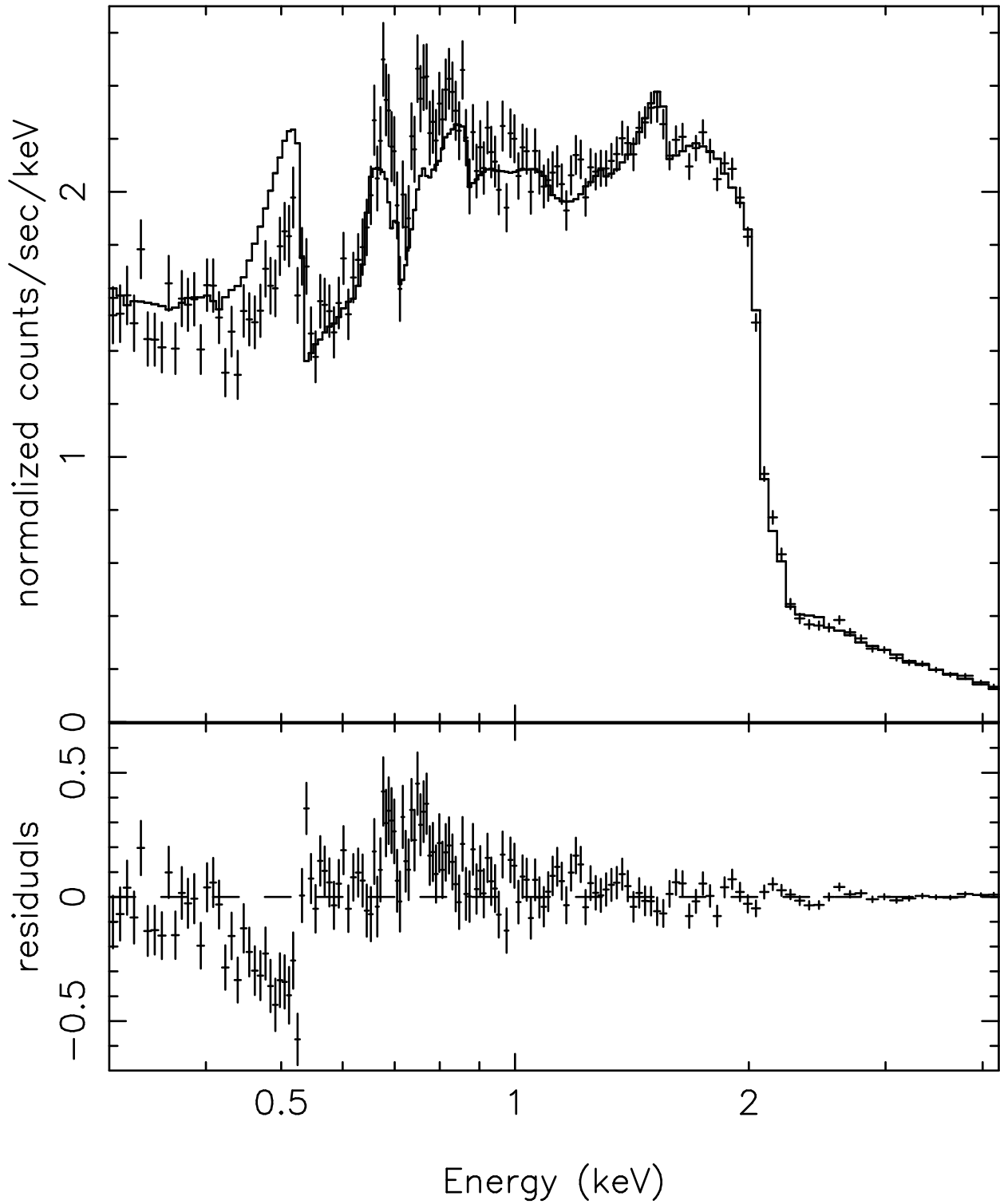


Fig. 3.— *Chandra*-LETGS spectrum of the Crab Pulsar compared to Model 1 (XSPEC *angr* abundances and *bcmc* cross-sections). Note the large residuals near the O_K edge (0.532 keV) that result in an unacceptable fit — $\chi^2 = 1722$ on 1553 degrees of freedom.

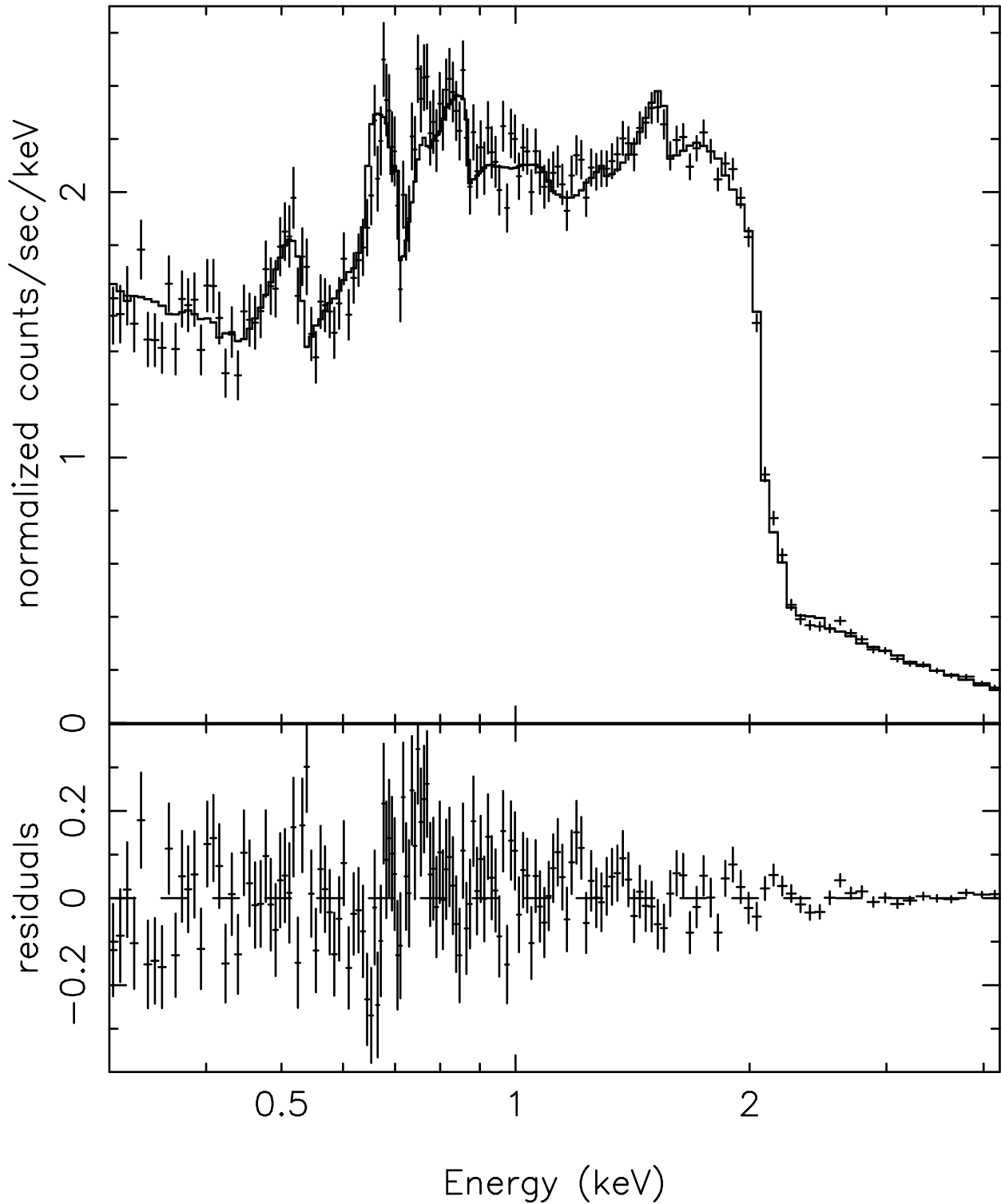


Fig. 4.— *Chandra*-LETGS spectrum of the Crab Pulsar compared to Model 2 (XSPEC *angr* abundances and *bcmc* cross-sections with thawed oxygen abundance). An acceptable fit — $\chi^2 = 1546$ on 1552 degrees of freedom — results if oxygen is underabundant with respect to *angr* values.

Table 1: XSPEC fits to *Chandra* LETGS (phase-integrated) spectrum of the Crab Pulsar.

Abundances ^a	Cross-sections ^b	χ^2/ν	Γ_{P}	N_{H} 10^{21} cm^{-2}	[O/H] 10^{-4}
Spectral fits without dust scattering					
angr	bcmc	1772/1553 ^c	^e	^e	8.51 ^f
angr	bcmc	1546/1552 ^d	1.596 ± 0.020	4.14 ± 0.12	3.45 ± 0.26
angr	obcm	1724/1553	^e	^e	8.51 ^f
angr	obcm	1542/1552	1.600 ± 0.020	3.77 ± 0.11	3.48 ± 0.30
angr	vern	1559/1552	1.611 ± 0.020	4.33 ± 0.12	3.93 ± 0.25
wilm	vern	1561/1553	1.549 ± 0.019	4.39 ± 0.08	4.90 ^f
wilm	vern	1540/1552	1.541 ± 0.019	4.84 ± 0.15	3.47 ± 0.24
wilm	tbvarabs	1551/1553	1.543 ± 0.019	4.24 ± 0.08	4.90 ^f
wilm	tbvarabs	1540/1552	1.536 ± 0.019	4.55 ± 0.15	3.76 ± 0.35
Spectral fits with dust scattering — $\tau_{\text{scat}} = 0.15$ at 1 keV					
angr	bcmc	1766/1553	^e	^e	8.51 ^f
angr	bcmc	1555/1552	1.643 ± 0.020	3.77 ± 0.12	3.18 ± 0.30
angr	obcm	1722/1553	^e	^e	8.51 ^f
angr	obcm	1551/1552	1.647 ± 0.020	3.43 ± 0.11	3.20 ± 0.34
angr	vern	1572/1552	1.655 ± 0.020	3.96 ± 0.12	3.56 ± 0.30
wilm	vern	1571/1553	1.601 ± 0.019	3.93 ± 0.08	4.90 ^f
wilm	vern	1540/1552	1.592 ± 0.019	4.46 ± 0.15	3.08 ± 0.28
wilm	tbvarabs	1558/1553	1.597 ± 0.019	3.80 ± 0.08	4.90 ^f
wilm	tbvarabs	1539/1552 ^g	1.587 ± 0.019	4.20 ± 0.14	3.33 ± 0.25

Note. —

^a Abundance models in XSPEC: **angr**, Anders & Grevesse (1989); **wilm**, Wilms, Allen, & McCray (2000)

^b Cross-section models in XSPEC: **bcmc**, Balucinska-Church & McCammon (1992) with He cross-section from Yan, Sadeghpour, & Dalgarno (1998); **obcm**, Balucinska-Church & McCammon (1992); **vern**, Verner et al. (1996); **tbvarabs**, Wilms et al. (2000, references therein) allowing for absorption by interstellar grains

^c Model 1 (see text and Fig. 3)

^d Model 2 (see text and Fig. 4)

^e “Best-fit” parameters and errors omitted for statistically poor fits

^f Default relative abundance of oxygen for the given abundance model

^g Model 3 (see text and Fig. 5), adopted for subsequent analyses

3.2. Broadband Spectrum — Further Analysis

Beyond the initial analysis (§3.1), we investigated effects on model fits and parameters using various combinations of cross-section and abundance models available within XSPEC. Besides the abundance model `angr` (§3.1), we considered `wilm` (Wilms, Allen, & McCray 2000). Besides the cross-section model `bcmc` (§3.1), we considered `obcm` (Baluncinska-Church & McCammon 1992, with old He cross-section), `vern` (Verner et al. 1996), and `tbvarabs` (Wilms et al. 2000). Wilms et al. (2000) employ updated abundances (Snow & Witt 1996; Cardelli et al. 1996; Meyer et al. 1997, 1998) and recent theoretical results for elemental absorption cross-sections (Band et al. 1990; Yan et al. 1998; Verner et al. 1993; Verner & Yakovlev 1995) and for molecular hydrogen (Yan et al. 1998). In addition, their cross-section models (XSPEC’s `tbabs` and `tbvarabs`) include effects on interstellar absorption due to condensation into grains, which becomes important for grains sufficiently large to be opaque at a given energy.

Owing to the small effective aperture of our observation, we deemed it prudent also to consider effects of (diffractive) scattering by grains upon interstellar extinction. Such scattering produces a wavelength-dependent X-ray scattering halo (Overbeck 1965; Mauche & Gorenstein 1986), related to the diffractive (half-power) angle $\vartheta_{\text{HP}} \approx 70'' / [(a/\mu\text{m})(E/\text{keV})]$. Consequently, for energies of interest here, all but the largest grains scatter outside the source extraction aperture, thus contributing to extinction. (See Takei et al. 2002 for another example of this effect.) Following Mauche & Gorenstein (1986), we calculate this scattering in the Rayleigh–Gans approximation (van der Hulst 1957; Overbeck 1965; Hayakawa 1970), valid when the phase shift through a grain diameter is small. This condition limits applicability to grains with radii

$$a \ll (0.5 \mu\text{m}) \left(\frac{E}{\text{keV}} \right) \left(\frac{\rho_{\text{grain}}}{\text{g cm}^{-3}} \right)^{-1} \left(\frac{2ZF(E)}{M} \right)^{-1}, \quad (1)$$

with ρ_{grain} the mass density of a dust grain and Z and M the summed atomic number and weight, respectively, of a grain-material molecule. The near-unity function $F(E) \equiv |\sum_i N_i f_i(E)| / (\sum_i N_i Z_i)$, with $f_i(E)$ the (complex) atomic scattering factor of atomic species i , N_i the number of species- i atoms per molecule, and Z_i the species- i atomic number.

In the Rayleigh–Gans approximation, the scattering depth is (Mauche & Gorenstein 1986)

$$\tau_{\text{scat}}(E) \equiv \tau_{\text{s1}} \left(\frac{F(E)}{F(1 \text{ keV})} \right)^2 \left(\frac{E}{\text{keV}} \right)^{-2}, \quad (2)$$

with τ_{s1} the dust scattering depth at 1 keV. For computations, we calculate $F(E)$ for the dust composition implied by the abundances and dust depletion factors given in Table 2

of Wilms et al. (2000), using atomic scattering factors from Henke et al. (1993). For the relevant case, which is extraction-aperture limited, a suitable fitting function, $N_E(E)$, for an power-law photon index spectrum is

$$N_E(E) = \text{constant} \times E^{-\alpha} \exp(-\tau_{\text{abs}}(E)) \exp(-\tau_{\text{scat}}(E)) , \quad (3)$$

with $\tau_{\text{abs}}(E)$ the photoelectric absorption depth and $\tau_{\text{scat}}(E)$ the scattering depth (Eq. 2).

For purposes of this study, we set $\tau_{s1} = 0.15$ and assume validity of the Rayleigh-Gans approximation, consistent with measurements of the Crab scattering halo (Mauche & Gorenstein 1989; Predehl & Schmitt 1995). We did not investigate more sophisticated grain-scattering models, because using the simple scattering model (Eq. 2) or ignoring scattering completely didn't affect the quality of the fits, most of which were statistically acceptable. Table 1 lists best-fit parameters and statistical errors (where the fit was statistically acceptable) for models ignoring and those including extinction due to scattering by interstellar grains. The first two table entries are Model 1 (Fig. 3) and Model 2 (Fig. 4) of the initial analysis (§3.1). The last entry is Model 3 (Fig. 5) which we consider to be astrophysically most accurate and thus adopt in subsequent analyses (§3.4 and §3.5).

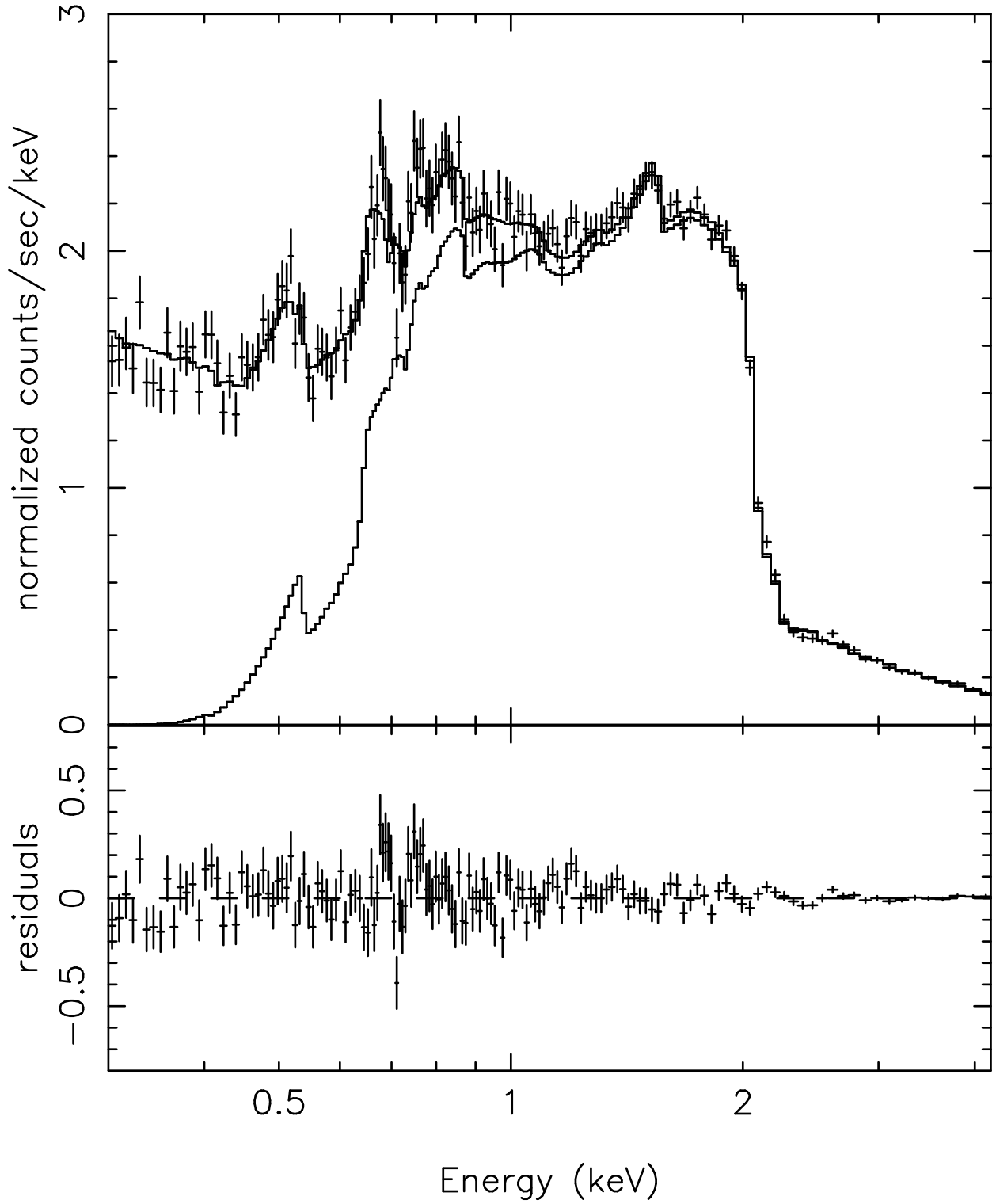


Fig. 5.— *Chandra*-LETGS spectrum of the Crab Pulsar compared to Model 3 (XSPEC `wilm` & `tbvarabs` with thawed oxygen abundance and with $\tau_{s1} = 0.15$, last entry in Table 1). This represents the preferred model, which serves as the basis for subsequent analyses. The lower solid line shows the model including only the first order response.

Inspection of Table 1 allows an assessment of the influence of the model upon the determination of the relevant parameters. In particular, we note the following:

1. Independent of the cross-section model, it is impossible to fit the data using the abundances of Anders & Grevesse (1989).
2. Models invoking the Anders & Grevesse (1989) abundances will fit the data if the oxygen is underabundant with a fractional abundance of 0.41 ± 0.07 .
3. If abundances recommended by Wilms et al. (2000) are used, the fits become acceptable independent of the various cross-sections used.
4. In all cases with statistically acceptable fits, the best-fit relative oxygen abundance is basically the same.
5. Using the Wilms et al. (2000) abundances with oxygen somewhat underabundant consistently gives a better fit than if the abundance is fixed at the nominal value.
6. Including extinction by dust scattering does not appreciably alter the quality of the fit; thus, while such extinction is expected, these spectral data do not require it.
7. Including dust scattering consistently modifies the best-fit parameters in an understandable way — the resulting photon index Γ_{p} is slightly flatter and the hydrogen column N_{H} and relative oxygen abundance $[\text{O}/\text{H}]$ are slightly lower.
8. The range of best-fit values for N_{H} substantially exceeds the statistical error of that parameter, demonstrating the importance of systematic uncertainties produced by using different cross-sections and/or abundances.

3.3. Broadband Spectrum — Comparison with Certain Previous Observations

Here we compare our measurements of the broadband spectrum with certain previous measurements — those taken with the *Einstein* Focal-Plane Crystal Spectrometer (FPCS) by Schattenburg & Canizares (1986), with the *Beppo-SAX* Low-Energy Concentrator Spectrometer (LECS) by Massaro et al. (2000), and with the *XMM-Newton* European Photon Imaging Camera (EPIC) by Willingale et al. (2001).

3.3.1. The *Einstein* measurements

Using the *Einstein* FPCS, Schattenburg & Canizares (1986) measured the spectrum of the Crab Nebula and its the pulsar, finding $N_{\text{H}} = (3.45 \pm 0.42) \times 10^{21} \text{ cm}^{-2}$ and $N_{\text{O}} = (2.78 \pm 0.42) \times 10^{18} \text{ cm}^{-2}$, giving a relative oxygen abundance $[O/H] = (8.1 \pm 1.6) \times 10^{-4}$. Because the measurements included all flux in a $6'$ field of view, they did not resolve the pulsar from the nebula. Their analysis did allow for the impact of flux scattered outside of the spectrometer’s $6'$ -diameter aperture upon the overall normalization. The model fitting of the *Einstein* data froze the nebula’s power-law index at $\Gamma_{\text{N}} = 2.1$ and used cross-sections and abundances from Morrison & McCammon (1983), but did not report the goodness of the fit.

If the quality of the fit were poor, statistical uncertainties in N_{H} and N_{O} may be underestimated, although the authors noted that they deliberately inflated the statistical errors in the data above 0.7 keV in their spectral fitting, perhaps to avoid this problem. In what follows, we shall first assume that the uncertainties are not underestimated. Before comparing results we note that their freezing the spectral index lowers the uncertainty relative to a fit with the spectral index left as a free parameter, but the differences may not be very large and their choice of spectral index (2.1) appears to be a very accurate value for the nebula-averaged index at low X-ray energies (see the discussion in §3.3.3). Similarly, we find for the *Chandra* data, e.g., that the uncertainty in N_{H} and N_{O} change by less than 10% depending on whether Γ is left as a free parameter or fixed at the best-fit value. Thus, if we compare the *Einstein*-derived values for the hydrogen column and the relative oxygen abundance with our measurements, we see that the values for N_{H} are similar within the errors, essentially independent of which cross-sections and abundances we used, whereas there appears to be a statistically significant discrepancy in the relative oxygen abundance. We shall see shortly (§ 3.3.2 & § 3.3.3) that this discrepancy is with all the more recent measurements. Moreover, Willingale et al. (2001) find that the column is rather uniform across the nebula (see §3.3.3), thus eliminating variations in the column as a possible reason for the discrepancy.

In order to try to understand the source of this discrepancy, we also compared the measured optical depths at the oxygen edge, which are directly related to the data independent of any models for abundance and cross-section.

Following Schattenburg & Canizares (1986), we omitted 2 of the 6 FPCS data points that lie closest to the oxygen edge as outliers, which they note are perhaps biased by neutral-oxygen K_α absorption and by the K edge of singly ionized oxygen. Scaling their quoted uncertainty in the fractional abundance of oxygen, we find $\tau_O = 1.6 \pm 0.3$. If we include all 6 FPCS data points in the analysis, we find $\tau_O = 0.8$, with a very poor fit ($\chi^2 = 15$ for 3 degrees of freedom). This leads us to conclude that had they included these points the value would have been smaller and the uncertainty in the optical depth larger. By way of comparison, we find for the *Chandra*-LETGS data that $\tau_O = 0.64 \pm 0.06$ in the direction of the pulsar. We also see no reason as to why the systematic errors that Schattenburg & Canizares (1986) applied to the data above 0.7 keV do not also apply below 0.7 keV. This would surely increase the uncertainty. As we have shown the FPCS result is sensitive to precisely which data is included in the fit, and, we suspect, to the precise modelling of the details of the spectral structure. We can only conclude that either the *Einstein*-FPCS uncertainties in the measured oxygen column (relative oxygen abundance) are underestimated or some systematic effect in the response has escaped detection.

3.3.2. The *Beppo-SAX* measurement

Massaro et al. (2000) used various *Beppo-SAX* instruments to measure the spectrum of the nebula and pulsar, which are spatially unresolved even using the *Beppo-SAX* X-ray concentrators. Of relevance to our measurements, the Low-Energy Concentrator Spectrometer (LECS) obtained a phase-resolved 0.1–4.0-keV spectrum of the nebula and pulsar. By analyzing the spectrum from the “low-pulse” phases, they minimize the pulsar contribution relative to the nebula.

T. Mineo kindly re-analyzed the *Beppo-SAX* LECS data, finding that underabundant oxygen substantially improved the fit ($\Delta\chi^2 = 48$ for 1 additional parameter) using the XSPEC `angr` abundances and `bcmc` cross-sections (cf. the second model of Table 1). This new fit gives $\Gamma_N = 2.06 \pm 0.08$, $N_H = (3.54 \pm 0.07) \times 10^{21} \text{ cm}^{-2}$, and $[O/H] = (6.25 \pm 0.33) \times 10^{-4}$; moreover, the fit was now marginally statistically acceptable with $\chi^2 = 428$ on 359 degrees of freedom. Thus, re-analysis of the *Beppo-SAX* data also indicates that oxygen in the Crab line of sight to be underabundant with respect to Anders & Grevesse (1989) abundances, however, not as much as our results.

3.3.3. The XMM-Newton measurement

Our final comparison is with the XMM-Newton observations reported by Willingale et al. (2001). Their analysis used 0.4–3.0-keV MOS-1 and -2 data, including data from the trailed (“out of time”) image, to fit five different data sets. The selected data sets isolated various Crab spatial structures — including the jet, the nebula as a whole, and the pulsar. The joint spectral fits to these data sets employed different power-law indices for each region but the same column density, with cross-sections from Balucinska-Church & McCammom (1992) plus newer He cross-section (Yan et al. 1998) and with abundances from Anders & Grevesse (1989).

Willingale et al. (2001) found statistically unacceptable fits before thawing both oxygen and iron abundances. Under the assumption that O and Fe have the same fractional abundance relative to solar, they determined the fractional abundance to be 0.63 ± 0.01 times solar (Anders & Grevesse 1989). These authors noted that the conclusion that oxygen may be underabundant is in agreement with earlier inferences from *Copernicus* data (e.g. Keenan, Hibbert, and Dufton 1985 and references therein). The best-fit parameters were $\Gamma_N = 2.108 \pm 0.006$, $\Gamma_P = 1.63 \pm 0.09$, $N_H = (3.45 \pm 0.02) \times 10^{21} \text{ cm}^{-2}$, and $[O/H] = (5.36 \pm 0.10) \times 10^{-4}$, with a $\chi^2 = 4007$ on $\nu = 3853$ degrees of freedom. In addition, by sampling $20'' \times 20''$ regions, Willingale et al. determined that column-density variations across the nebula are small.

We examined our data to determine whether we could confirm an underabundance of iron. Using our preferred model (Model 3, Table 1), we thawed 5 XSPEC parameters — the power-law index, its normalization, the hydrogen column density, the fractional abundance of O, and individually the fractional abundance of He, C, N, Na, Mg, Al, Si, Cl, Ar, Ca, Cr, Fe, and Co. Here the fractional abundance is the ratio of the abundance of a given element to its standard (default) abundance. For nearly all these elements, the *Chandra*-LETGS spectroscopy was insensitive up to a fractional abundance from Wilms et al.(2000) of at least 2. The exceptions with regards to the sensitivity were helium and iron with fractional abundances of 1.07 ± 0.20 and 0.77 ± 0.18 , respectively. These to be compared with an oxygen fractional abundance of 0.68 ± 0.05 already discussed. Therefore, in all cases, except for the oxygen, our results were consistent with normal abundances relative to the reference. The uncertainty and the trend in the relative iron abundance is consistent with it being either normal (with respect to Wilms et al. 2000) or low, and tied to that of oxygen. We therefore conclude that our results are qualitatively consistent with those of Willingale et al. (2001), although we disagree as to the degree of the oxygen underabundance. There are no easy ways to account for the discrepancy. Both analyses agree within statistical errors on the hydrogen column, when the same models for cross sections and abundances are used.

Willingale et al. (2001) did not account for scattering by the ISM which tends to lower the estimated relative oxygen abundance (see Table 1) but it is difficult to see that this would be a very large factor, especially since the *XMM-Newton* beam is so much larger than that of *Chandra*. A significant difference between the two experiments is the spectral resolution, in that Willingale et al. (2001) used CCDs. It is possible that the better *Chandra*-LETGS spectral resolution, especially with regards to details of the oxygen edge, might account for the discrepancy. It is of course possible that the *Chandra* response is in error, but the good fit of the pulsar spectrum to the powerlaw model seems to indicate that the model is correct. We note that the LETGS response was *not* calibrated using the Crab. Future experiments that deal with the accuracy of the calibration of the instruments will be necessary to clarify the details.

3.4. Spectral Variation with Pulse Phase

In principle, repeating the previous analysis for the time-tagged data (appropriately arranged by pulse phase) provides a phase-resolved measurement of the pulsar’s spectral parameters. However, a HRC-S timing error assigns to each event the time of the previous event, thus complicating the analysis for this bright source because telemetry saturation omits events from the telemetry stream. In Tennant et al. (2001), we discussed this problem and a method for maintaining timing accuracy — albeit at significantly reduced (here, by a factor of 15) data-collection efficiency. This method filters the data accepting only telemetered events separated by no more than 2 ms, guaranteeing a timing accuracy never worse than 2 ms and typically much better. Jodrell Bank (Lyne, Pritchard, & Smith 1993) routinely observes the Crab Pulsar (Wong, Backer, & Lyne 2001); providing a period ephemeris (<http://www.jb.man.ac.uk/~pulsar/crab.html>). Roberts & Kramer (2000, private communication) kindly prepared an ephemeris matched to our observation times. Applying the 2-ms filter and folding the data according to the radio ephemeris we found that the X-ray flux peaks at phase 0.984 as discussed in Tennant et al. (2001).

In performing the phase-resolved spectral analysis, we used interstellar absorption and dust scattering parameters of our preferred XSPEC model (Model 3, last entry of Table 1 and Figure 5). Table 2 and Figure 6 summarize the results for the pulsar’s phase-resolved photon index Γ_{P} . Note that for each phase range, the power-law fit is statistically acceptable without requiring an additional spectral component.

Table 2: Spectral Parameters versus Pulse Phase. Uncertainties for the photon index Γ_{P} are $1\text{-}\sigma$ statistical errors.

Phase range	Γ_{P}	χ^2/ν
0.01–0.06	1.71 ± 0.07	32.9/37
0.06–0.10	1.53 ± 0.20	20.7/15
0.10–0.20	1.53 ± 0.15	35.1/35
0.20–0.30	1.50 ± 0.09	61.3/46
0.30–0.35	1.43 ± 0.07	30.7/35
0.35–0.42	1.54 ± 0.04	74.1/82
0.42–0.45	1.72 ± 0.11	16.6/18
0.45–0.55	1.78 ± 0.16	39.0/34
0.55–0.70	$1.4^{+1.0}_{-1.3}$	36.2/41
0.70–0.82	2.9 ± 1.0	34.9/34
0.82–0.90	1.47 ± 0.63	35.6/24
0.90–0.95	1.48 ± 0.08	29.9/31
0.95–0.01	1.61 ± 0.03	132/105

Based upon a χ^2 analysis of the distribution of best-fit photon indices (Table 2), we reject (albeit at only 85% confidence) the hypothesis that the spectral index is constant with phase. (The error-weighted average of the spectral indices was 1.58 and the value of χ^2 was 16.8 on 12 degrees of freedom.) The apparent variation of spectral index between pulse phases -0.1 and 0.5 is qualitatively similar in *Chandra*, *Beppo-SAX* (Massaro et al. 2000), and *Rossi-XTE* (Pravdo, Angelini, & Harding 1997) measurements, with the index increasing (becoming softer) through the two pulse maxima and decreasing (becoming harder) in the bridge between the pulses. However, only *Chandra* provides the angular resolution needed to isolate the pulsar from the nebula in order to measure the spectral index for the pulse-phase range 0.5–0.9. Our analysis is consistent with an apparent continuation of the increase (softening) of the spectral index until just before the onset of the primary pulse; however, the data do not require this. Due to the HRC time-tag problem, the efficiency of the *Chandra* observation was low (5.5%); hence, the spectral-index uncertainty near pulse minimum is large. We have proposed a much more efficient approach for collecting *Chandra*-LETGS data from the Crab Pulsar, which would significantly reduce statistical uncertainties without expending inordinate observing time. These future observations would directly challenge theoretical models for pulsar emission (e.g., Zhang & Chen 2002).

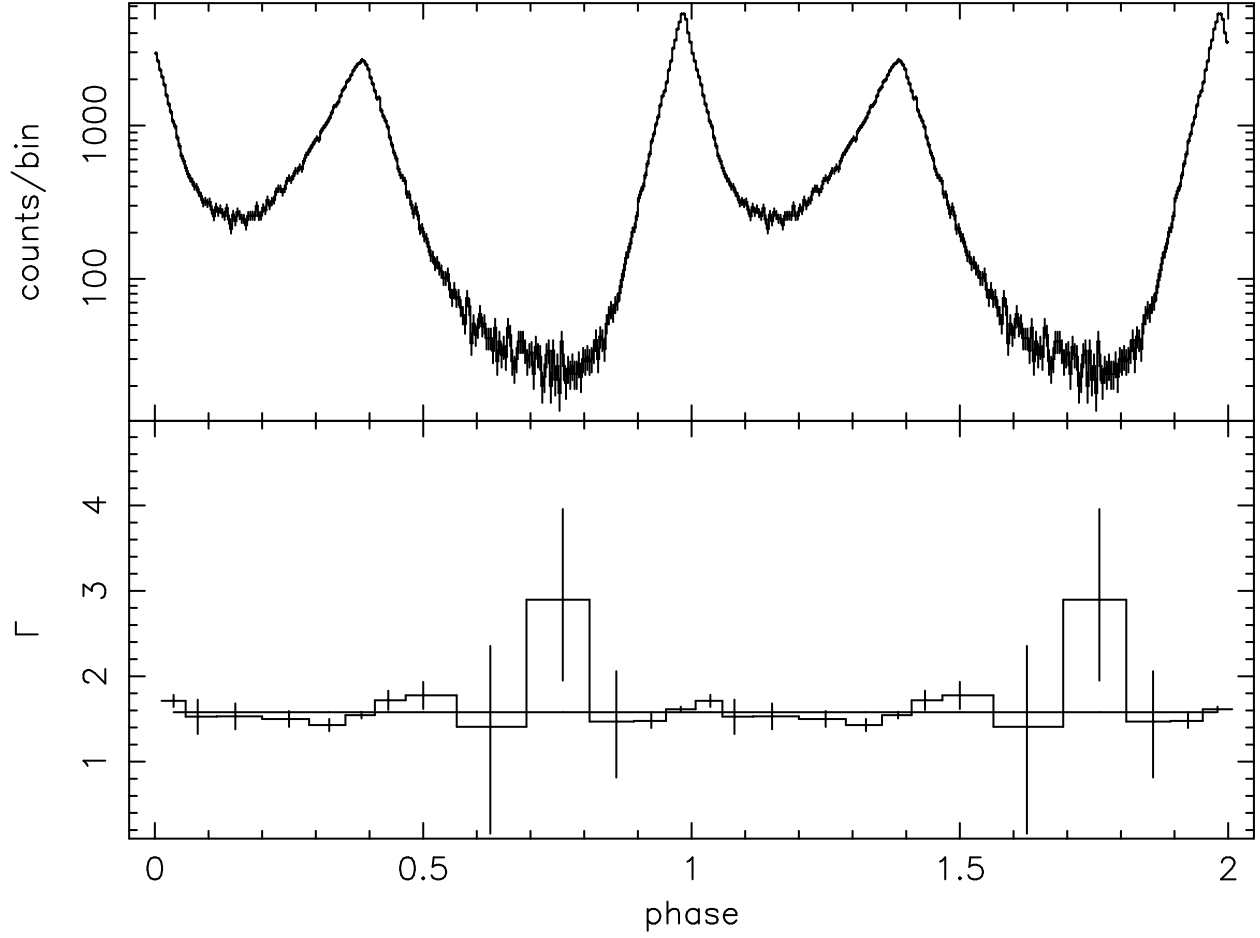


Fig. 6.— Crab Pulsar light curve and photon index as a function of pulse phase. Note that the plots span two (identical) pulse cycles.

3.5. Temperature of the Neutron Star

Here we investigate adding a blackbody component to the spectral fits in order to set an upper limit to the temperature of the underlying neutron star. Ideally, data taken at pulse minimum would provide the most stringent upper limit. In practice, however, the phase-averaged data (which do not require time-interval filtering) yield the best limit due to their much better photon statistics. Figure 7 shows a portion of the confidence contours of the blackbody normalization (θ_∞^2) versus blackbody temperature (kT_∞) using the preferred model (`wilm` and `tbvrabs`) with $\tau_{s1} = 0.15$, but Γ_P , N_H , and $[O/H]$ thawed. Here θ_∞ is the angular size determined by a distant observer, in XSPEC units — $\theta_\infty = (R_\infty/D_{10})$, with R_∞ the stellar radius in km units and D_{10} the source distance in 10-kpc units.

The best fit (not shown in the figure) gave $kT = 187$ keV and $\theta_\infty^2 = 0.0018$, $[\text{km}/(10 \text{ kpc})]^2 = [8.5 \text{ m}/(2 \text{ kpc})]^2$, with $\chi^2 = 1537$ on 1550 degrees of freedom. Clearly, the best-fit parameters — corresponding to a radius of less than 10 meters — cannot represent thermal emission from the entire surface of a neutron star, although they might indicate a very small, very hot spot on the surface. It is more reasonable, however, that the best-fit high temperature and low normalization are indicative of the absence of any thermal component. Figure 7 shows the upper portions of the “banana” plot for contours consistent with blackbody emission from the entire neutron-star surface. To utilize these contours, we assume the properties (equation of state, mass, radii, etc.) for a $1.358-M_\odot$ neutron star with $R_\infty = 15.6$ km — appropriate for models that assume neutron-star cores with moderately stiff equations of state and containing strong proton superfluidity (e.g., Kaminker, Haensel, & Yakovlev 2001; Kaminker, Yakovlev, & Gnedin 2002 and references therein). For a Crab distance of 2 kpc, the contours (Fig. 7) imply a (2- σ , 3- σ) upper limit to the (gravitationally-redshifted) blackbody surface temperature viewed at infinity of $T_\infty < (1.85, 1.97)$ MK [$\log T_\infty < (6.27, 6.30)$]. This upper limit is slightly less than the one we (Tennant et al. 2001) previously obtained using only the zero-order counting rate — no spectral data — from a longer observation. More difficult to quantify are consequences of departures from uniform, isotropic, blackbody emission (e.g., Pavlov et al. 1994; Zavlin et al. 1995; Pavlov 2000; Becker & Pavlov 2001). Hence, we regard T_∞ as a representative and indicative upper limit.

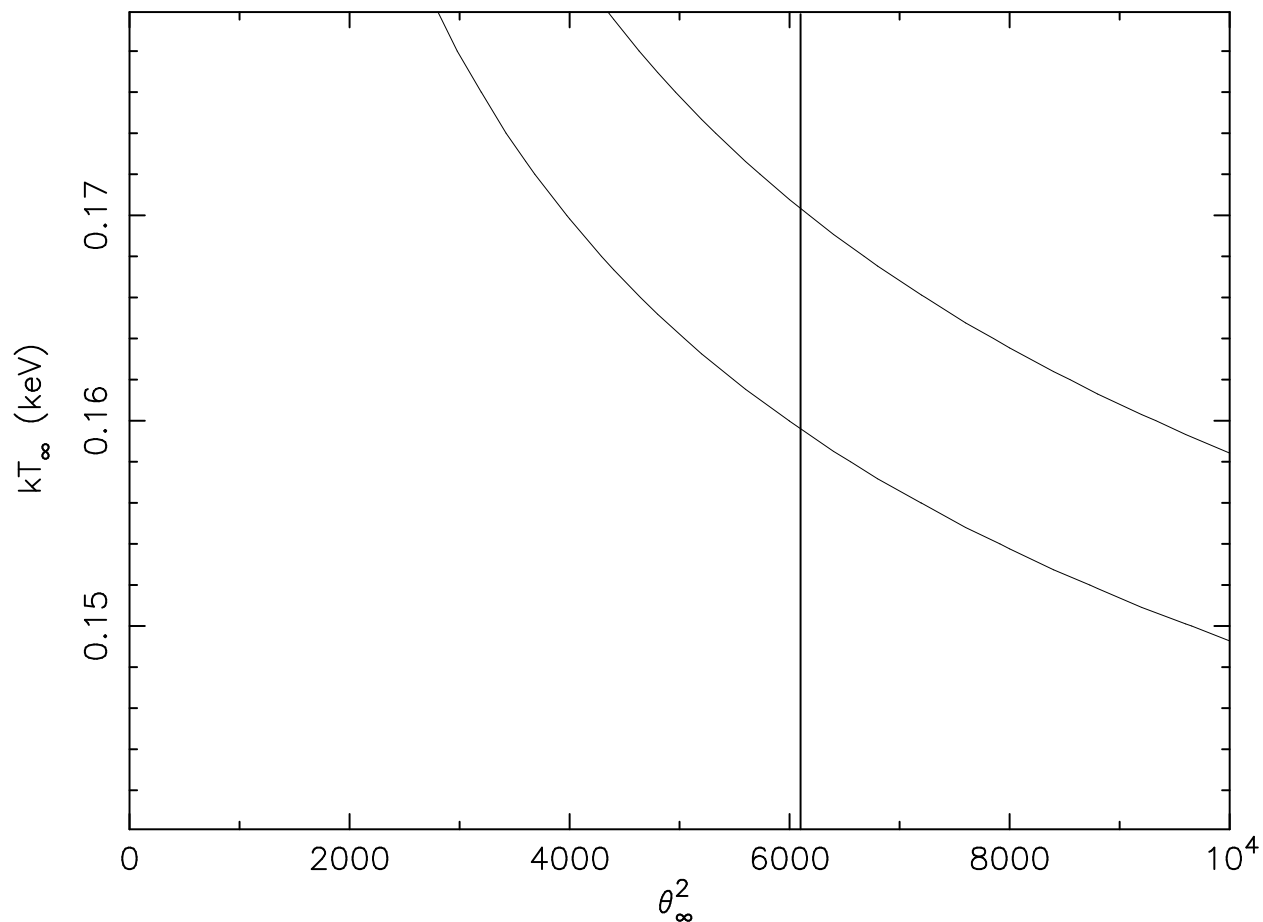


Fig. 7.— Outer confidence contours of the neutron-star surface temperature versus blackbody normalization. The (lower, upper) contour denotes the the upper limit at (95.4%, 99.7%) confidence — $\Delta\chi^2 = \chi^2 - \chi_{\min}^2 = (4.0, 9.0)$, corresponding to the single-parameter (2- σ , 3- σ) upper limit. For reference, our canonical neutron star has a blackbody normalization $\theta_\infty^2 = 6100$ [km/(10 kpc)]².

4. Summary

We have computed and compared the measurements of the phase-averaged spectrum of the Crab Pulsar using a variety of cross-sections and abundances. We have shown that results are somewhat sensitive to the abundances and cross-sections used in the analysis. This is especially true for the hydrogen column and emphasizes the importance of specifying which cross-sections and abundances are assumed in the data analysis. We have also compared our results with a number of previous observations. Although we confirm the results first derived from *Copernicus* data (Keenan, Hibbets, & Dufton 1985 and references therein) and more recently of Willingale et al. (2001) that the Crab line-of-sight is underabundant in oxygen, our analysis of the *Chandra*-LETGS data suggests a somewhat greater hydrogen column and a smaller (factor of 0.6) relative oxygen abundance than this previous analysis. The increased hydrogen column we measure is primarily due to the choice of cross-sections and abundances, whereas the lower relative oxygen abundance we attribute to the better spectral resolution and calibration accuracy of the *Chandra* LETGS. In addition, we have measured for the first time the spectrum of the Crab Pulsar as a function of pulse phase at all pulse phases. We find marginal evidence for variation of the power law spectral index, but the statistics at and near pulse minimum are limited. Future, more precise, measurements are needed. In all our analyses, we have accounted for the contribution of scattering by interstellar dust to the extinction of X rays in an aperture-limited measurement — a consideration in spectral analysis of point sources observed with *Chandra*'s exceptional angular resolution. Finally, we used the spectral data to obtain a new and better upper limit to the temperature of the neutron star of $\log T_\infty < 6.30(3 - \sigma)$.

We thank the referee for detailed and insightful comments. We also acknowledge a tremendous debt to Leon Van Speybroeck for his remarkable contributions to the development of the *Chandra* optics. His untimely death has touched us all.

REFERENCES

- Anders, E., & Ebihara, M. 1982, *Geochimica et Cosmochimica Acta*, 46, 2363
Anders, E., & Grevesse, N. 1989, *Geochimica et Cosmochimica Acta*, 53, 197
Arnaud, K. A. 1996, in *Astronomical Data Analysis software Systems V*, eds. G. Jacoby & J. Barnes (ASP Conf. Ser. 101), 17
Balucinska-Church, M. & McCammon, D. 1992, *ApJ*, 400, 699
Band, I. M., Trzhaskovskaya, M. B., Verner, D. A., & Yakovlev, D. G. 1990, *A&A*, 237, 267

- Becker, W., & Pavlov, G.G. 2001, in *The Century of Space Science*, eds. J.A.M. Bleeker, J. Giess, & M.C.E. Huber (Dordrecht: Kluwer Academic Publishers), 721
- Cardelli, J. A., Meyer, D. M., Jure, M., & Savage, B. D. 1996, *ApJ*, 467, 334
- Chiang, J., & Romani, R. W.. 1994, *ApJ*, 436, 754
- Daugherty, J. K. & Harding, A. K. 1996, *ApJ*, 458, 278
- Hayakawa, S. 1970, *Prog. Theor. Phys.*, 43, 1224
- Henke, B. L., Gullikson, E. M., & Davis, J. C. 1993, *Atomic Data & Nuclear Data Tables*, 54, 181
- Kaminker, A. D., Haensel, P., & Yakovlev, D. G. 2001, *A&A*, 373, L17
- Kaminker, A. D., Yakovlev, D. G., & Gnedin, O. Y. 2002, *A&A*, 383,1076
- Keenan, F. P., Hibbert, A., & Dufton, P. 1985, *Astr. Ap.*, 147, 89.
- Lyne A. G., Pritchard R. S. & Smith F. G., 1993, *MNRAS*, 265, 1003
- Margon, B., 1974, *Nature*, 249, 24
- Massaro, E., Cusumano, G., Litterio, M., & Mineo, T. 2000, *A&A*,361, 695
- Mauche, C. W., & Gorenstein, P. 1986., *ApJ*, 302, 371
- Mauche, C. W., & Gorenstein, P. 1989., *ApJ*, 336, 843
- McLaughlin, B. M., & Kirby, K. P. 1998, *J. Phys. B: At. Mol. Opt. Phys.*, 31, 4991
- Meehan, G. R., et al. 1997, *proc. SPIE*, 3114, 74
(available on <http://hea-www.harvard.edu/HRC/calib/spie97.html>)
- Meyer, D. M., Cardelli, J. A., & Sofia, U. J. 1997, *ApJ*, 490, L103
- Meyer, D. M., Jura, M., & Cardelli, J. A. 1998, *ApJ*, 493, 222
- Morrison, R., & McCammon, D. 1983, *ApJ*, 270, 119
- Overbeck, J. W. 1965, *ApJ*, 141, 864
- Pavlov, G. G., Shibanov, Y. A., Ventura, J., & Zavlin, V. E. 1994, *A&A*, 289, 837
- Pavlov, G. G., Zavlin, V. E., Aschenbach, B., Trümper, J., &Sanwal, D. 2000, *ApJ*, 531, L53
- Pravdo, S. H., Angelini, L., & Harding, A. K. 1977, *ApJ*, 491, 808
- Predehl, P., & Schmitt, J. H. M. M. 1995, *A&A*, 293, 889
- Romani, R. W. 1996, *ApJ*, 470, 469
- Romani, R. W., & Yadigaroglu, I.-A. 1995, *ApJ*, 438, 314
- Schattenburg, M. L., & Canizares, C. R. 1986, *ApJ*, 301, 759

- Snow, T. P., & Witt, A. N. 1996, ApJ, 468, L65
- Sturmer, S. J. & Dermer, C. D. 1994, ApJ, 420, L79
- Takei, Y., Fujimoto, R., Mitsuda, K., & Onaka, T. 2002, ApJ, 581, 307
- Tennant, A.F., Becker, W., Juda, M., Elsner, R. F., Kolodziejczak, J. J., Murray, S. S., O'Dell, S. L., Paerels, F., Swartz, D. A., Shibasaki, N., & Weisskopf, M. C. 2001, ApJ, 554, L173
- Toor, A., & Seward, F. D. 1974, AJ, 79, 995
- Toor, A., & Seward, F. D. 1977, ApJ, 216, 560
- van der Hulst, H. C. 1957, Light Scattering by Small Particles (New York: Dover)
- Verner, D. A., & Yakovlev, D. G. 1995, A&AS, 109, 125
- Verner, D. A., Yakovlev, D. G., Band, I. M., & Trzhaskovskaya, M. B 1993, Atomic Data & Nuclear Data Tables, 55, 233
- Wong, T., Backer, D. C., & Lyne, A. G. 2001, ApJ, 548, 447
- Willingale, R., Aschenbach, B., Griffiths, R. G., Sembay, S., Warwick, R. S., Becker, W., Abbey, A. F., & Bonnet-Bidaud, J.-M. 2001, A&A, 365, L212
- Wilms, J., Allen, A., & McCray, R. 2000, ApJ, 542, 914
- Yan, M., Sadeghpour, H. R., & Dalgarno, A. 1998, ApJ, 496, 1044
- Zavlin, V. E., Pavlov, G. G., Shibanov, Y. A., & Ventura, J. 1995, A&A, 297, 441
- Zhang, L. & Cheng, K. S. 2002 ApJ, 569, 872